ADVANCED FUNCTIONAL MATERIALS
www.afm-journal.de

A Self-Standing High-Performance Hydrogen Evolution Electrode with Nanostructured $NiCo_2O_4$/CuS Heterostructures

*Li An, Liang Huang, Panpan Zhou, Jie Yin, Hongyan Liu, and Pinxian Xi**

An efficient self-standing 3D hydrogen evolution cathode has been developed by coating nickel cobaltite ($NiCo_2O_4$)/CuS nanowire heterostructures on a carbon fiber paper (CFP). The obtained CFP/$NiCo_2O_4$/CuS electrode shows exceptional hydrogen evolution reaction (HER) performance and excellent durability in acidic conditions. Remarkably, as an integrated 3D hydrogen-evolving cathode operating in acidic electrolytes, CFP/$NiCo_2O_4$/CuS maintains its activity more than 50 h and exhibits an onset overpotential of 31.1 mV, an exchange current density of 0.246 mA cm^{-2}, and a Tafel slope of 41 mV dec^{-1}. Compared to other non-Pt electrocatalysts reported to date, CFP/$NiCo_2O_4$/CuS exhibits the highest HER activity and can be used in HER to produce H_2 with nearly quantitative faradaic yield in acidic aqueous media with stable activity. Furthermore, by using CFP/$NiCo_2O_4$/CuS as a self-standing electrode in a water electrolyzer, a current density of 18 mA cm^{-2} can be achieved at a voltage of 1.5 V which can be driven by a single-cell battery. This strategy provides an effective, durable, and non-Pt electrode for water splitting and hydrogen generation.

1. Introduction

Hydrogen generation from water splitting represents an important strategy to address the global energy problem.[1] Hydrogen evolution reaction (HER) involving the electrocatalytic reduction of protons to molecular hydrogen in acidic solutions is an important half reaction used in water splitting coupled with oxygen evolution reaction (OER).[2] To drive the HER with high energetic efficiency, the use of a powerful catalyst which can minimize the over potential is essential.[3] Pt-based catalysts are the most common and active materials used for the HER, but their high cost and scarcity greatly restrict their industrial application.[4] Promising water splitting devices, based on the proton exchange membrane[5] technology, rely on noble metal-based catalysts.[6] While these precious metals are the most effective catalysts, their large-scale application is hampered by the scarcity and consequent high cost.[7] Therefore, to make H_2 as a competitive energy source, it is crucial to develop highly efficient and robust HER catalysts based on abundant materials. Recent reports have shown that metal oxides based on cobalt and nickel metals are robust electrocatalysts for water oxidation (OER).[8] However, a few of such oxides are used as catalysts for hydrogen evolution (HER). Given that metallic cobalt has a low energy barrier for hydrogen adsorption,[9] it is highly possible that Co-based composites are promising HER catalysts. As one of the mixed valence oxides of Co, nickel cobaltite ($NiCo_2O_4$) exhibits good OER performance with lower overpotential and Tafel slope than crystalline oxides,[10] the HER performance of $NiCo_2O_4$ has been rarely investigated. Inspired by these results, we synthesized a self-standing 3D heterostructure cathode on carbon fiber paper (CFP) by incorporating $NiCo_2O_4$ nanowires (NWs) with CuS nanocrystal (NC) and explored its potential to be used as HER catalysts.

$NiCo_2O_4$ self-standing NWs are synthesized because their large surface area can facilitate effective mass transfer[11] and burst the larger hydrogen gas bubbles that commonly pin at the surface of film electrodes, and thus maintain the solid–liquid interface.[12] It has been shown that the integrity of $NiCo_2O_4$ NWs cannot be maintained when used as electrodes after several electrocatalytic cycles. Transition-metal chalcogenides (TMCs) have been widely investigated as catalysts or supports for application in the HER because of their low costs, high chemical stability, and high electrocatalytic properties.[13,14] Both theoretical[15] and experimental[16] studies concluded that the HER activity arises from the sites located along the edges of the TMC layers which indicates the unsaturated sulfur atoms on the edges play a crucial role in HER catalysis.[17] As a typical TMC, CuS (covellite) possesses a layered crystal structure with weak van der Waals interactions between individual

L. An, Dr. P. Zhou, J. Yin, Dr. H. Liu, Prof. P. Xi
Key Laboratory of Nonferrous Metal Chemistry and Resources Utilization of Gansu Province
State Key Laboratory of Applied Organic Chemistry and The Research Center of Biomedical Nanotechnology
Lanzhou University
Lanzhou 730000, P. R. China
E-mail: xipx@lzu.edu.cn

Dr. L. Huang
Wuhan National Laboratory for Optoelectronics
School of Optical and Electronic Information
Huazhong University of Science and Technology
Wuhan 430074, P. R. China

DOI: 10.1002/adfm.201503784

planar Cu_2S_2 double layers.[18] Because of its anisotropic structure, CuS can offer permeable channels for ion adsorption and transport.[19] Meanwhile, for their empty 3p-orbitals in sulfur and the presence of rich electron holes in the structure, CuS has a strong tendency to capture electrons and to promote electron-transfer reactions with electron donor molecules with low onset reduction potential and high current.[20] These properties make CuS especially suitable as an HER catalyst, however their catalytic activity toward the HER has rarely been investigated. To address this issue, we deposited a layer of CuS NCs on $NiCo_2O_4$ NWs to form $NiCo_2O_4$/CuS NW heterostructure.[21] It is expected that the layered structure of CuS can offer permeable channels for ion adsorption and transportion.[22] The performance of CFP/$NiCo_2O_4$/CuS NW heterostructure cathode for HER was evaluated. Remarkably, CFP/$NiCo_2O_4$/CuS NWs show a good HER catalytic activity, close to that of commercial Pt/C catalysts. Furthermore, their HER activity can be maintained at least 50 h under acidic conditions with a faradaic efficiency (FE) of nearly 100%. These findings open up new possibilities to develop highly efficient and robust bifunctional catalysts based on low-cost materials.

2. Results and Discussion

A two-step strategy was used to fabricate CFP/$NiCo_2O_4$/CuS NWs, as illustrated in **Scheme 1**. First, $NiCo_2O_4$ NWs were hydrothermally grown on CFP according to a previously reported method,[23] followed by chemically coating CuS NCs on CFP/$NiCo_2O_4$ by a low-temperature sulfurization reaction (see the Experimental Section for details). **Figure 1**a shows the X-ray diffraction (XRD) patterns of CFP, CFP/$NiCo_2O_4$, CFP/CuS, and CFP/$NiCo_2O_4$/CuS. All the diffraction peaks of CFP/$NiCo_2O_4$ (purple curve) can be indexed according to the cubic $NiCo_2O_4$ with a space group of $Fd\ \bar{3}m$ (JCPDS Card No. 73-1702). The peaks of CFP/CuS (blue curve) indicate hexagonal CuS with a space group of $P63/mmc$ (JCPDS Card No. 06-0464). All of the diffraction peaks in CFP/$NiCo_2O_4$ and in CFP/CuS were observed in CFP/$NiCo_2O_4$/CuS (red curve), suggesting the formation of the heterostructure where the CFP (typical morphology shown in Figures S1 and S2, Supporting Information) offers the skeleton for the growth of the $NiCo_2O_4$/CuS NW heterostructure. The formation of the $NiCo_2O_4$/CuS NW heterostructure is further confirmed by the scanning electron microscope (SEM) images (Figure 1b,c). After coating CuS NCs on the CFP/$NiCo_2O_4$ NWs, the CFP/$NiCo_2O_4$/CuS NWs formed without destroying the NW structure (Figure 1c). The high-resolution transmissiom electron microscopy (HR-TEM) image of CFP/$NiCO_2O_4$/CuS (Figure 1d) shows lattice fringes with interplane spacing of 0.28 nm and 0.24 nm, corresponding to the (103) plane of CuS and the (311) plane of the $NiCo_2O_4$ NCs, respectively. The selective area electron diffraction (SAED) pattern (Figure 1e) shows several bright rings made up of discrete spots, which can be indexed to the (110), (101), and (103) planes of a hexagonal CuS structure, and the (311), (220), and (400) planes of a cubic $NiCo_2O_4$ structure. As illustrated in Figure 1f, the SEM image and the corresponding elemental mapping images further confirmed the formation of CFP/$NiCO_2O_4$/CuS NWs in which all elements were uniformly distributed in the system. From the mapping area, it can be seen that the carbon element is present in the CFP skeleton. The Ni, Co, and O elemental images revealed that $NiCo_2O_4$ NWs were distributed across the whole CFP. The Cu and S elemental images suggested the presence of CuS nanostructures. The energy dispersive X-ray spectrum verified that the Cu:S and Ni:Co atomic ratios were ≈1:1 and 1:2, respectively (Figure S3, Supporting Information).

The chemical composition of CFP/$NiCo_2O_4$/CuS NWs was further analyzed by X-ray photoelectron spectra (XPS). An elemental survey of XPS indicates the presence of Co, Ni, O, Cu, S, and C elements in CFP/$NiCo_2O_4$/CuS NWs (Figure S4, Supporting Information), consistent with SEM results. The C 1s peaks are 284.6 eV (**Figure 2**a) originated from the CFP. The Ni 2p spectra (Figure 2b) consist of two spin–orbit doublets characteristics of Ni^{2+} and Ni^{3+} and two shakeup satellites (indicated as "Sat."). Similarly, the Co 2p spectra (Figure 2c) are composed of two spin–orbit doublets characteristics of Co^{2+} and Co^{3+} and two shakeup satellites. The O1s spectra (Figure 2d) show four oxygen contributions, denoted as O1 (529.9 eV), O2 (530.6 eV), O3 (531.7 eV), and O4 (533.8 eV), which associate with the typical of metal–oxygen bond, the oxygen in hydroxyl groups, the high number of defect sites with low oxygen coordination in the material with small particle size, and the multiplicity of physi-/chemisorbed water at and within the surface, respectively.[24] The binding energies of Cu $2p_{3/2}$ and Cu $2p_{1/2}$ peaks are 932.1 and 951.9 eV (Figure 2e), respectively. In addition, the symmetrical shapes of the two Cu 2p XPS peaks and the "shakeup" satellite peaks in the higher binding-energy ranges imply the presence of pure CuS. Figure 2f shows the XPS of S 2p, the peaks at 162.5 and 161.3 eV assigned to the binding energies of S $2p_{1/2}$ and S $2p_{3/2}$, respectively, which are separated by a spin–orbit splitting of 1.2 eV. The Raman spectroscopy was further used to characterize the structure of CFP/$NiCo_2O_4$/CuS NWs. As displayed in **Figure 3**, the peaks at 186, 480, 529, and 668 cm^{-1} correspond to the F_{2g}, E_g, F_{2g}, and A_{1g} models of the $NiCo_2O_4$ NWs, respectively.[25] After CuS coating, a new peak at 472 cm^{-1} was observed, corresponding to the well-known A_{1g} model for CuS. Another CuS signature at 263 cm^{-1} is also observed,[26] confirming the coating of CuS. These results all suggest that CFP/$NiCo_2O_4$/CuS NWs were successfully fabricated.

To investigate the conduction band energy (E_c) and valence band energy (E_v) of CFP/$NiCo_2O_4$, CFP/CuS, and CFP/$NiCo_2O_4$/CuS, ultraviolet photoelectron spectroscopy (UPS) (Figure S5, Supporting Information) and UV–vis spectrum

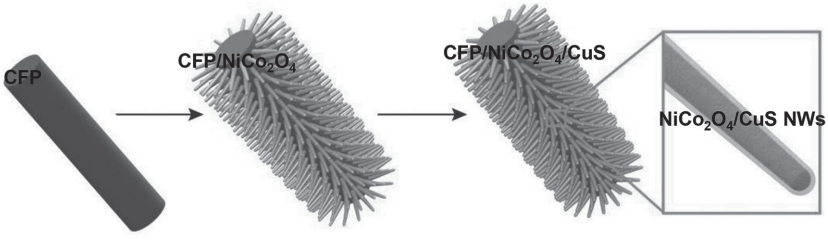

Scheme 1. The strategy for the fabrication of CFP/$NiCo_2O_4$/CuS NWs.

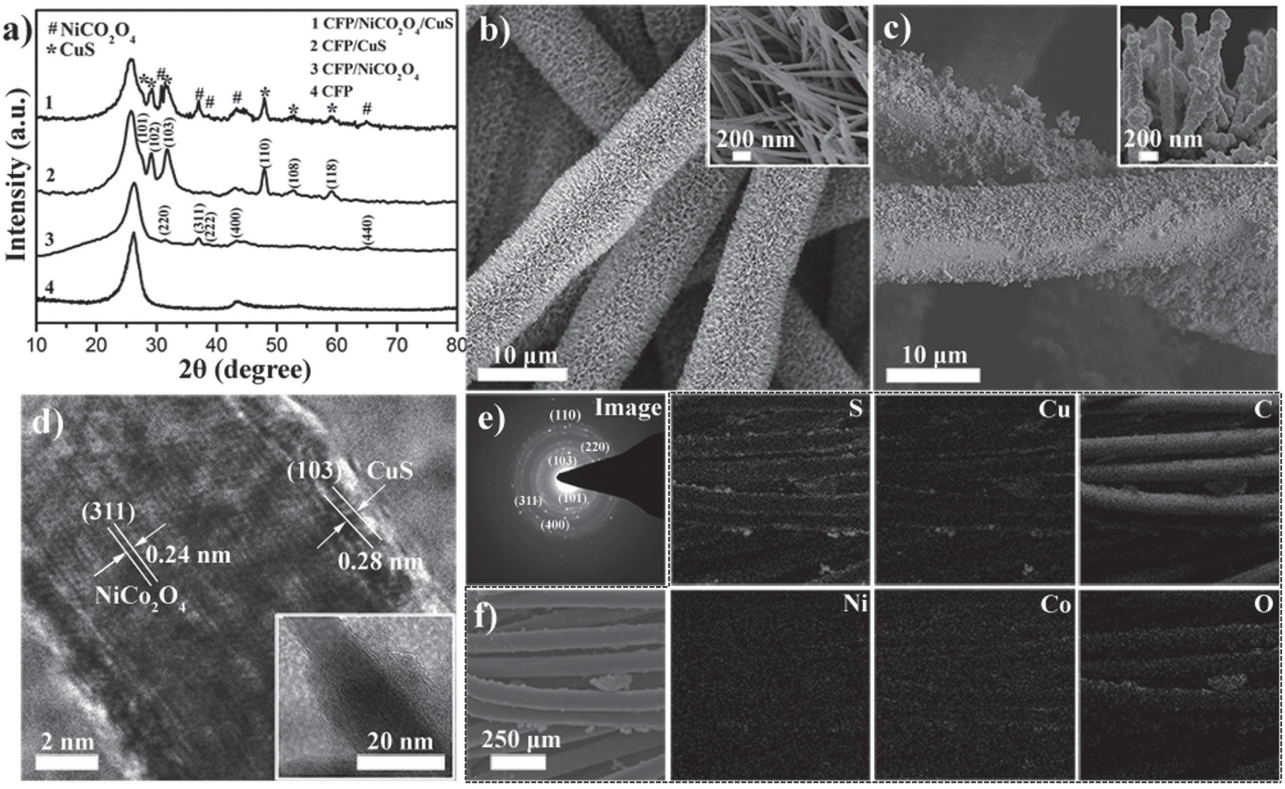

Figure 1. a) XRD patterns of CFP, CFP/$NiCo_2O_4$, CFP/CuS, and CFP/$NiCo_2O_4$/CuS. b) Low- and high-magnification (inset) SEM images of CFP/$NiCo_2O_4$. c) Low- and high-magnification (inset) SEM images of CFP/$NiCo_2O_4$/CuS. d) HRTEM and TEM images (inset) of CFP/$NiCo_2O_4$/CuS. e) SAED pattern of CFP/$NiCo_2O_4$/CuS. f) SEM image and EDS elementals mapping images of S, Cu, C, Ni, Co, and O for CFP/$NiCo_2O_4$/CuS.

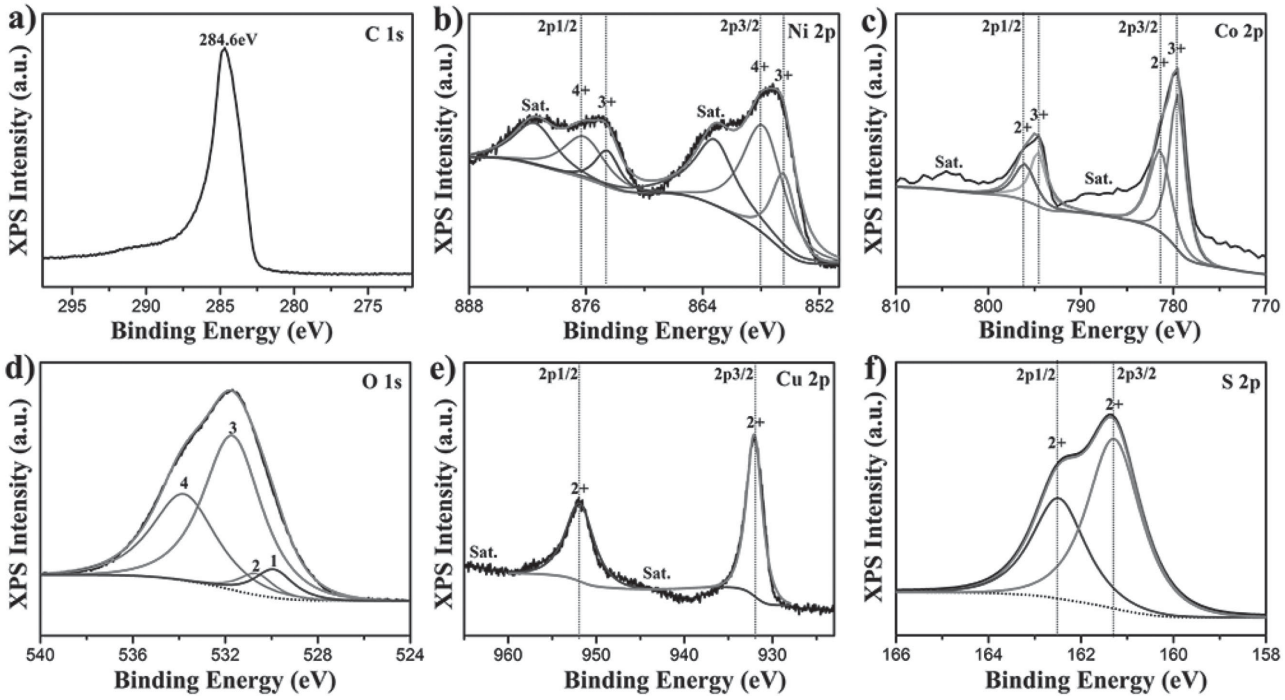

Figure 2. XPS spectra in the a) C (1s), b) Ni (2p), c) Co (2p), d) O (1s), e) Cu (2p), and f) S (2p) regions survey spectrum for CFP/$NiCo_2O_4$/CuS.

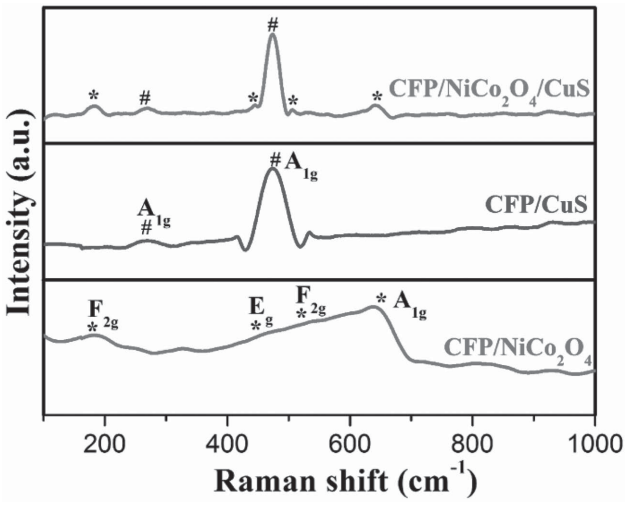

Figure 3. Raman spectra of CFP/$NiCo_2O_4$, CFP/CuS, and CFP/$NiCo_2O_4$/CuS.

analysis (Figure S6, Supporting Information) were performed. The calculated E_c, E_v, and E_g of CFP/$NiCo_2O_4$, CFP/CuS, and CFP/$NiCo_2O_4$/CuS are listed in **Table 1**. It can be found that the band gap of CFP/$NiCo_2O_4$/CuS (2.86 eV) was much smaller than that of CFP/$NiCo_2O_4$ (3.30 eV) after the CuS coating (Table 1), which can be ascribed to the enhanced hybridization during the formation of the $NiCo_2O_4$/CuS heterostructures which could lead to more charge carriers and higher intrinsic conductivity.[27] The band gap of CFP/$NiCo_2O_4$/CuS are properly positioned to permit transfer of electrons and holes, which can be used for water splitting.[28]

The catalytic performance of CFP/$NiCo_2O_4$/CuS NWs for HER was evaluated by using linear sweep voltammetry (LSV). LSV measurement was conducted in a three-electrode system in 0.5 M H_2SO_4 with a scan rate of 2 mV s^{-1}. Commercial Pt/C catalysts (20 wt% Pt on Vulcan carbon black) loaded on CFP and bare CFP were also examined for comparison. Because as-measured reaction currents do not directly reflect the intrinsic behavior of the catalysts due to the effect of ohmic resistance (iR), an iR correction was applied to all initial data. **Figure 4**a compares the polarization curves for different electrodes. The Pt/C electrode exhibits the expected HER performance with negligible overpotential, while the bare CFP showed very low HER activity. It is interesting to note that the CFP/$NiCo_2O_4$/CuS self-standing electrode exhibits a much smaller onset overpotential (31.1 mV) compared to CFP/CuS (298 mV) and CFP/$NiCo_2O_4$ (317 mV) (Figure 4b). Furthermore, a rapid rise of cathodic current was observed at more negative potential in CFP/$NiCo_2O_4$/CuS electrode, suggesting the excellent performance of the CFP/$NiCo_2O_4$/CuS as a 3D cathode in generating H_2 via water splitting. As can be seen from **Table 2**, to achieve a current density of 10 mA cm^{-2}, the requirement of an overpotential for CFP/$NiCo_2O_4$/CuS was 72.3 mV, while a larger overpotential of 449 mV (524 mV) was required for the CFP/CuS (CFP/$NiCo_2O_4$) electrode. Furthermore, for the CFP/$NiCo_2O_4$/CuS, an overpotential of 105.2 mV was needed to achieve a current density of 100 mA cm^{-2}. By contrast, these overpotentials for CFP/$NiCo_2O_4$/CuS were superior to most reported values

Table 1. Comparison of E_c, E_v, and E_g of CFP/$NiCo_2O_4$, CFP/CuS, and CFP/$NiCo_2O_4$/CuS.

Catalyst	E_c [eV]	E_v [eV]	E_g [eV]
CFP/$NiCo_2O_4$	4.67	7.97	3.30
CFP/CuS	4.77	7.91	3.14
CFP/$NiCo_2O_4$/CuS	4.74	7.60	2.86

for non-Pt HER catalysts in acidic aqueous media (Table S1, Supporting Information).

Figure 4c shows the iR-corrected Tafel plots, overpotential versus log (j), for CFP/$NiCo_2O_4$, CFP/CuS, and CFP/$NiCo_2O_4$/CuS. The Tafel plot for Pt/C is also presented for comparison. The linear portions of the Tafel plots are fitted to the Tafel equation ($\eta = b \log j + a$), where j is the current density, b is the Tafel slope, and a is the intercept relative to the exchange current density (j_0),[29] from which Tafel slopes of 30, 41, 144, 165, and 269 mV dec^{-1} were yielded for Pt/C, CFP/$NiCo_2O_4$/CuS, CFP/CuS, CFP/$NiCo_2O_4$, and CFP, respectively. The Pt/C electrode exhibited a Tafel slope of ≈30 mV dec^{-1} and an exchange current density of 0.72 mA cm^{-2}, which is consistent with the reported value.[30] The Tafel slopes for the CFP/$NiCo_2O_4$/CuS catalysts nearly matched the expected Tafel slopes of 39 mV dec^{-1}, revealing that the HER proceeded via a Volmer–Heyrovsky mechanism ($H_3O^+ + e^- = H_{ads} + H_2O$ and $H_{ads} + H_3O^+ + e^- = H_2 + H_2O$).[30] The exchange current density (j_0) of CFP/$NiCo_2O_4$/CuS was ≈0.246 mA cm^{-2}, which was eight times higher than that of CFP/CuS and 23 times higher than that of CFP/$NiCo_2O_4$ (Table 2 and Figure 4d). This value was also higher than those of the HER catalysts reported in the literature (Table S1, Supporting Information).

To prove the better balance between the intrinsic and interdomain conductivity for CFP/$NiCo_2O_4$, CFP/CuS, and CFP/$NiCo_2O_4$/CuS in the HER process, electrochemical impedance spectroscopy was performed to investigate the electrode kinetics in HER (Figure 4e). After the formation of $NiCo_2O_4$/CuS heterostructures, the nyquist plots revealed a remarkable decrease in the charge-transfer resistance (R_{CT}) from 321.4 Ω (CFP/$NiCo_2O_4$) to 6.302 Ω (CFP/$NiCo_2O_4$/CuS) (Table S2, Supporting Information), which indicates a decrease in reaction resistance. A significant decrease of R_{CT} values for CFP/$NiCo_2O_4$/CuS indicates a smaller reaction resistance and higher catalytic activity for HER in acid solution on CFP/$NiCo_2O_4$/CuS electrode.[31]

In addition to its high HER activity, the durability of the CFP/$NiCo_2O_4$/CuS self-standing electrode was assessed. As shown in Figure 4f, after continuous cyclic voltammograms (CV) scanning in 0.5 M H_2SO_4 with a scan rate of 2 mV s^{-1}, the curve measured after 8000 CV cycles shows negligible difference with the initial curve, indicating the excellent durability of the CFP/$NiCo_2O_4$/CuS self-standing electrode during long-term cycling. The inset of Figure 4f shows that the CFP/$NiCo_2O_4$/CuS electrode exhibits a very slow degradation in catalytic current during the operation and retained 92% of current density after 50 h. Interestingly, big spikes in the HER current were observed for the chronoamperometric response. This might be attributed to the consumption of H^+ or the accumulation of H_2 bubbles on the electrode surface which may hinder

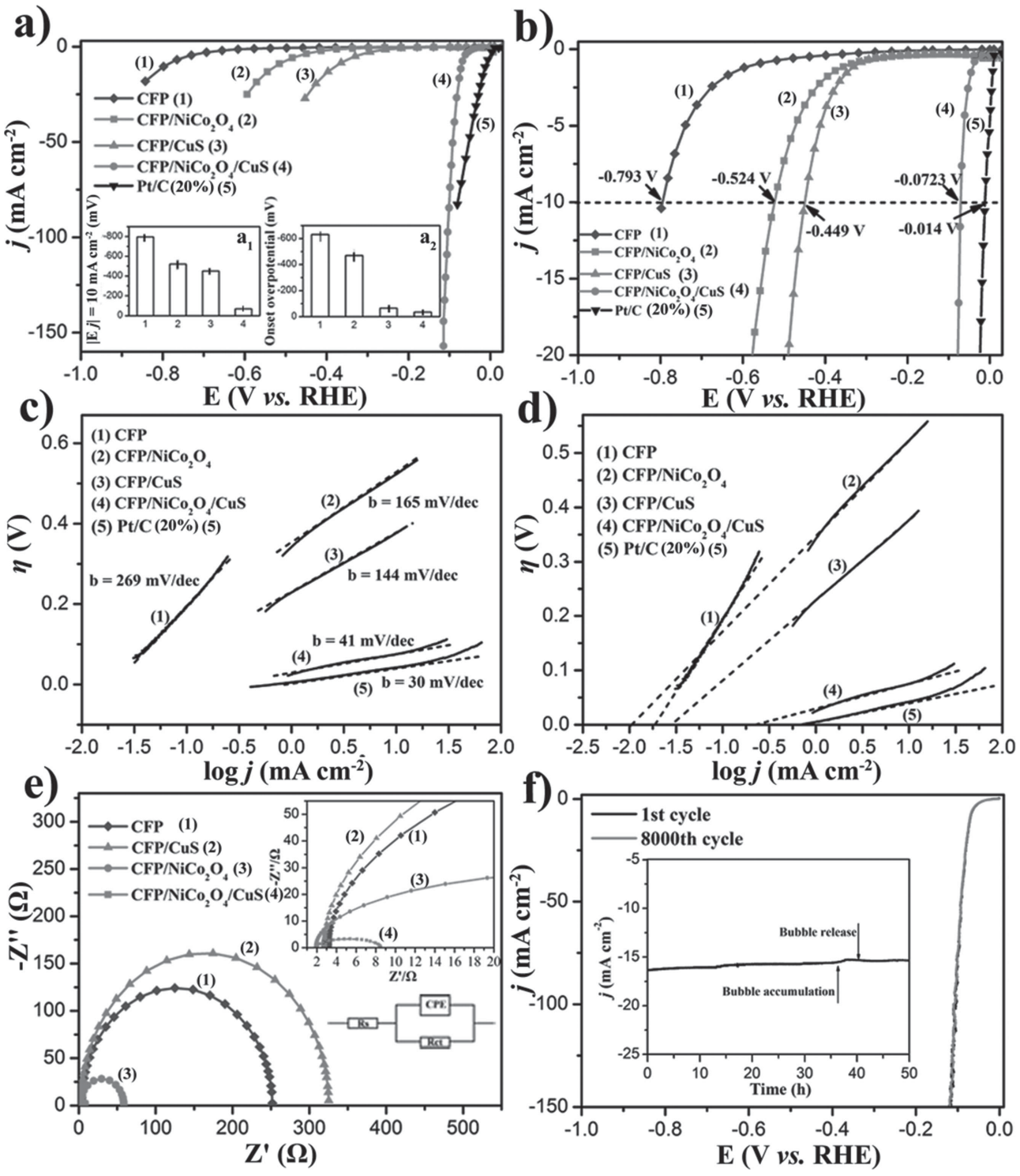

Figure 4. a) Polarization curves of CFP, CFP/CuS, CFP/$NiCo_2O_4$, CFP/$NiCo_2O_4$/CuS, and Pt/C in 0.5 M H_2SO_4 with a scan rate of 2 mV s^{-1}. Inset a_1: The potential histograms at the current density of 10 mA cm^{-2}. Inset a_2: Onset overpotential histograms for CFP, CFP/CuS, CFP/$NiCo_2O_4$, and CFP/$NiCo_2O_4$/CuS. Error bars represent the standard deviations of CFP, CFP/CuS, CFP/$NiCo_2O_4$, and CFP/$NiCo_2O_4$/CuS for three measurements. b) Polarization curves of CFP, CFP/$NiCo_2O_4$, CFP/CuS, CFP/$NiCo_2O_4$/CuS, and Pt/C in 0.5 M H_2SO_4 with a scan rate of 2 mV s^{-1}. c) Tafel plots of CFP, CFP/CuS, CFP/$NiCo_2O_4$, CFP/$NiCo_2O_4$/CuS, and Pt/C. d) Calculated exchange current density for CFP, CFP/$NiCo_2O_4$, CFP/CuS, CFP/$NiCo_2O_4$/CuS, and Pt/C in 0.5 M H_2SO_4 by applying the extrapolation method to the Tafel plot. e) Nyquist plots of each sample. Inset in (e): The corresponding Nyquist plot at the high-frequency range. f) Polarization curves for CFP/$NiCo_2O_4$/CuS before and after 8000 cycles between –0.03 V and +0.42 V versus RHE at a scan rate of 100 mV s^{-1} in 0.5 M H_2SO_4. Inset in (f): Time-dependent current density curve for the CFP/$NiCo_2O_4$/CuS at a static overpotential of 200 mV for 50 h.

Table 2. Comparison of HER activity data for different catalysts.

Catalyst	Onset overpotential [V vs RHE]	η at j = 10 mA cm^{-2} [V vs RHE]	Tafel slope [mV dec^{-1}]	Exchange current density [mA cm^{-2}]
CFP	0.556	−0.793	269	0.0192
CFP/$NiCo_2O_4$	0.317	−0.524	144	0.0107
CFP/CuS	0.298	−0.449	165	0.0294
CFP/$NiCo_2O_4$/CuS	0.0311	−0.0723	41	0.246
Pt/C	0.0184	−0.0140	30	0.724

the reaction.[32] After 50 h operation, XPS studies revealed no obvious chemical state change of S 2p, Cu 2p, C 1s, Ni 2p, Co 2p, and O 1s in the CFP/$NiCo_2O_4$/CuS (Figure S7, Supporting Information). The SEM elemental mapping of the CFP/$NiCo_2O_4$/CuS also confirmed the existence of all the elements and their positions (Figure S8, Supporting Information), suggesting the robustness of this self-standing electrode. From the durability study, it was found that the CFP/$NiCo_2O_4$/CuS electrode was inherently stable for HER due to the stable structure of the $NiCo_2O_4$/CuS heterostructure coated on CFP.

To gain insight into the intrinsic catalytic activity of CFP/$NiCo_2O_4$/CuS, the turnover frequency (TOF) for each active site was estimated using methods previously reported.[33] The number of active sites was examined by CV in a pH = 7 phosphate buffer with a scan rate of 50 mV s^{-1}. Figure S9a (Supporting Information) shows the CVs of CFP/$NiCo_2O_4$/CuS and the bare glass carbon electrode (GCE) in the range of −0.2 to 0.6 V versus RHE. The number of active sites on the catalyst modified GCE was calculated to be 1.73×10^{-7} mol. The calculated TOFs are shown in Figure S9b (Supporting Information). As the most active catalyst, Pt/C showed a TOF of 0.8 s^{-1} at η = 0 mV.[34] To achieve a TOF of 0.725 s^{-1}, CFP/$NiCo_2O_4$/CuS needed an overpotential of ≈84 mV, much smaller than that required for defect-rich MoS_2 (300 mV).[35] For a TOF of 4 s^{-1}, an overpotential of 180 mV was needed, which was 60 mV smaller than self-supported nanoporous cobalt phosphide NW arrays (240 mV).[36] Potentiostatic cathodic electrolysis was performed by maintaining the CFP/$NiCo_2O_4$/CuS at an overpotential of 250 mV for 120 min. By comparing the amount of measured hydrogen with calculated hydrogen (assuming 100% FE), we observed an FE close to 100% for the hydrogen evolution (**Figure 5**). As a result, the CFP/$NiCo_2O_4$/CuS which possessed rich and effective active sites determined the superior HER activity, suggesting the achievement of synergistically structural and electronic modulations for HER catalysis.

To reveal the correlation of the structure of CFP/$NiCo_2O_4$/CuS electrode with its enhanced electrocatalytic HER performance, the greatly improved HER performance of the CFP/$NiCo_2O_4$/CuS heterostructures was assessed by XPS measurements, the peaks at 780.9 and 779.9 eV (**Figure 6**) correspond to the Co $2p_{3/2}$ of CFP/$NiCo_2O_4$ and CFP/$NiCo_2O_4$/CuS, respectively. It can be seen that the electron binding energy of the Co $2p_{3/2}$ had a 1.0 eV decrease after loading with CuS. This was due to the close assembly and strong interaction between the CuS and $NiCo_2O_4$, finally resulting in the impaired electron density of the Co atoms in the CFP/$NiCo_2O_4$. Additionally, the incorporated CuS also caused the impaired electron density of the Co atoms, making the Co more nucleophilic.

The superior catalytic performance and stability of the CFP/$NiCo_2O_4$/CuS cathode can be attributed to the following factors: 1) the direct integration of $NiCo_2O_4$ NWs onto CFP enables efficient mass transfer and good mechanical adhesion; 2) the formation of $NiCo_2O_4$/CuS heterostructures reduces the band gap and causes the electronic structure change of the $NiCo_2O_4$, thus enhancing the intrinsic conductivity of nanodomains and facilitating the combination between positive protons and catalysts; 3) CuS has a low K_{sp} (8.5×10^{-45}), and its high crystallinity ensures that it is very stable during long-term electrocatalysis in acidic conditions; 4) the self-standing feature of the CFP/$NiCo_2O_4$/CuS avoids the use of binder which may block active sites and inhibit diffusion.[37]

In view of these advantages of the CFP/$NiCo_2O_4$/CuS cathode, we further investigated its application as a water reduction catalyst in an electrolyzer. The experiment was carried out

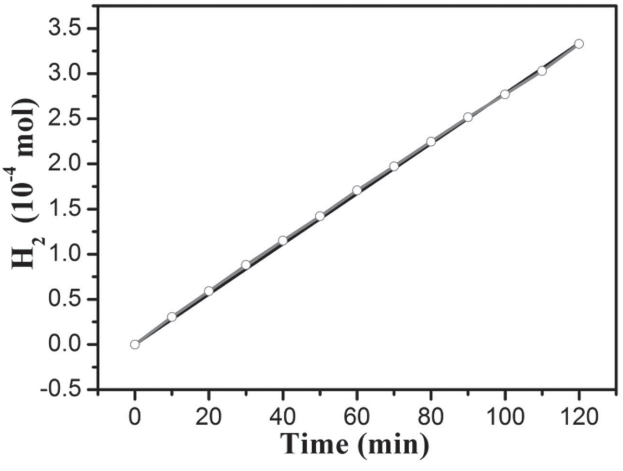

Figure 5. The amount of theoretically calculated (black line) and experimentally measured (line with dots) hydrogen versus time for CFP/$NiCo_2O_4$/CuS at an overpotential of 250 mV for 120 min.

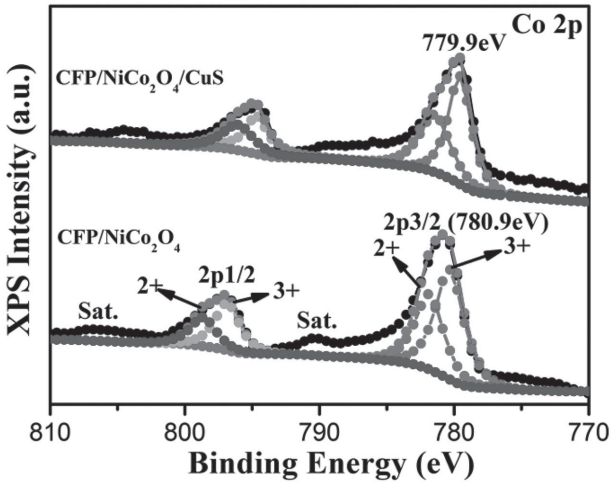

Figure 6. Co 2p XPS spectra for CFP/$NiCo_2O_4$ and CFP/$NiCo_2O_4$/CuS.

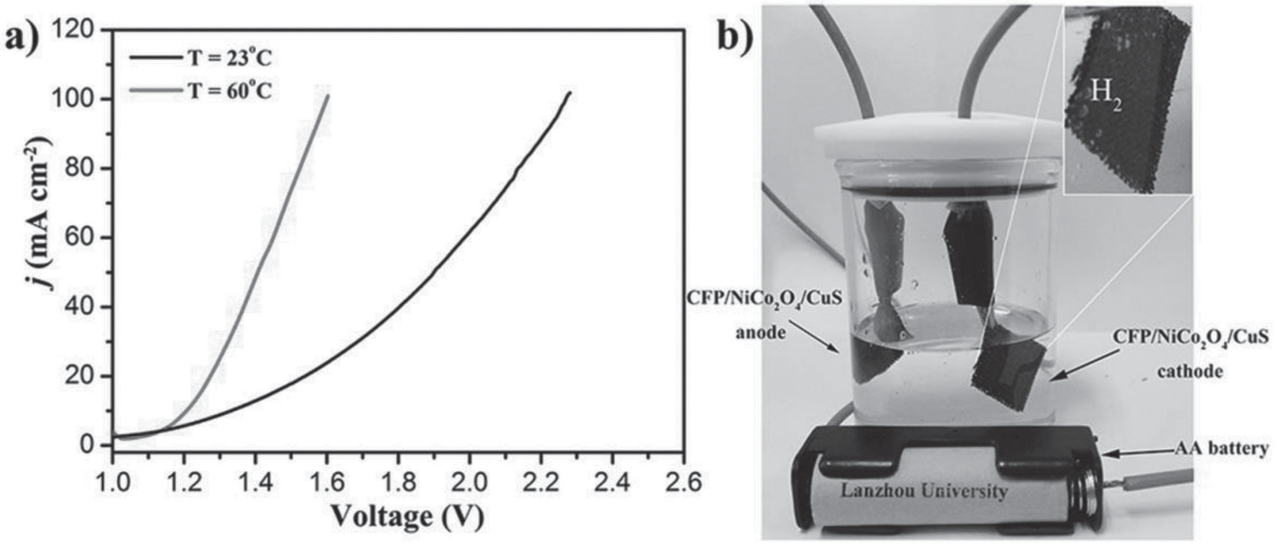

Figure 7. a) Linear sweepment voltammetry of water electrolysis using CFP/$NiCo_2O_4$/CuS as HER and OER catalyst in 0.5 M H_2SO_4 at different temperatures. b) Demonstration of a water-splitting device powered by an AA battery with a nominal voltage of 1.5 V.

at room temperature (≈23 °C) and ≈60 °C in 0.5 M H_2SO_4. Water electrolysis with a low current density of 18 mA cm^{-2} at ≈1.50 V and a high current density of 100 mA cm^{-2} at ≈2.26 V was observed at room temperature (**Figure 7**a). The kinetics and thermodynamics were greatly improved at high temperature (≈60 °C), showing a lower voltage of ≈1.25 V at 18 mA cm^{-2} and a higher current increase, reaching 100 mA cm^{-2} at a voltage of ≈1.59 V (Figure 7a) with a good stability (Figure S10, Supporting Information). Such water electrolysis could be powered by a single-cell AA battery with a nominal voltage of <1.5 V (Figure 7b and see Supporting Information Movie for a video of water electrolysis by an AA battery). These results suggested that the CFP/$NiCo_2O_4$/CuS heterostructure can match the benchmark Pt/C catalyst for efficient electrolyzers with low overpotential for water-splitting devices.

3. Conclusion

In summary, the nanostructured $NiCo_2O_4$/CuS heterostructure attached to CFP network has been developed as a novel self-standing electrode, and it exhibited a highly efficient HER performance with a low overpotential and a large exchange current density, comparable to or even better than Pt-free and other fabricated metallic catalysts. A small Tafel slope of 41 mV dec^{-1} suggests a Volmer–Heyrovsky mechanism for the catalyzed HER. These findings can be attributed to an increased abundance of the exposed catalytic edge sites and excellent electrical coupling to the CFP/$NiCo_2O_4$/CuS self-standing electrodes. An efficient electrolyzer achieving a current density of 18 mA cm^{-2} at a voltage of 1.5 V was demonstrated. These remarkable features together with the self-standing nature of CFP/$NiCo_2O_4$/CuS make it promising in practical use as water-splitting devices. The work presented in this paper will encourage the research on improving the activity of various electrocatalysts by synergistical structure and electronic modulations.

4. Experimental Section

Material Synthesis: Preparation of $NiCo_2O_4$ NWs array on the CFP: First, self-supported $NiCo_2O_4$ NWs were prepared by a facile hydrothermal synthesis method. In a typical procedure, 1.33 g $Co(NO_3)_2$•$6H_2O$, 0.66 g $Ni(NO_3)_2$•$6H_2O$, and 0.48 g urea were dissolved in 160 mL deionized (DI) water. After stirred for ≈20 min, a transparent pink colored solution was obtained. The solution was transferred into a 200 mL Teflon-lined stainless steel autoclave. Two pieces of CFP (3 × 4 cm^2) vertically inserted into the Teflon holder were subsequently soaked in the solution followed by heating the solution to 120 °C in an electric oven and kept at that temperature for 16 h. The as synthesized electrodes were then taken out, ultrasonically cleaned for 5 min in the DI water and rinsed with ethanol several times, dried at 80 °C overnight, and annealed at 300 °C in air for 2 h to get the CFP/$NiCo_2O_4$. The mass loading of $NiCo_2O_4$ NWs on CFP was 0.3 mg cm^{-2}.

Preparation of CFP/$NiCo_2O_4$/CuS: 0.34 g $CuCl_2$•$2H_2O$ and 0.025 g sodium dodecylbenzene sulfonate were dissolved in 100 mL DI water. The CFP (3 × 4 cm^2) loaded with $NiCo_2O_4$ was put into the above solution by heating in water bath at 100 °C for 4 h. Afterward, 0.45 g thioacetamide dissolved in 50 mL DI was added and kept at 100 °C for ≈4 h. Finally, the CFP/$NiCo_2O_4$/CuS was obtained and cleaned with the DI water and ethanol several times, dried in vacuum at 50 °C overnight.

Structural Characterizations: Powder XRD patterns were collected on a Rigaku D/Max-2400 diffractometer with Cu-Kα radiation (λ = 1.54178 Å). TEM images, HRTEM images, SAED, and energy disperse X-ray spectrum (EDS) were taken with a Tecnai G2 F30 field emission transmission electron microscope. The SEM images and scan SEM images were taken with a field-emission scanning electron microscope (Hitachi, S4700 FESEM system) with an ultimate image resolution of 1.2 nm at 25 kV. The XPS measurement was obtained on a PHI-5702 multifunctional spectrometer using Al Kα radiation.

Hydrogen Evolution Activity Test: Electrochemical measurements were carried out in a typical three-electrode glass cell connected to a CHI 760 E Electrochemical Workstation (CHI Instruments, Shanghai Chenhua Instrument Corp., China) at a scan rate of 2 mV s^{-1} in an electrolyte solution of 0.5 M H_2SO_4. The synthesized CFP/$NiCo_2O_4$, CFP/CuS, and CFP/$NiCo_2O_4$/CuS were directly used as the working electrode for electrochemical characterizations. Saturated Ag/AgCl (in a saturated KCl solution) was employed as a reference electrode, and a Pt net was employed as an auxiliary electrode. In 0.5 M H_2SO_4, the Ag/AgCl electrode was calibrated with respect to reversible hydrogen electrode

(RHE): $E_{RHE} = E_{Ag/AgCl} + 0.197$ V. LSV was conducted in 0.5 M H_2SO_4 with a scan rate of 2 mV s^{-1}. The time dependency of catalytic currents during electrolysis for the catalyst was tested in 0.5 M H_2SO_4 at $\eta = 200$ mV after equilibrium. In this work, all electrochemical experiments were carried out at 20 ± 0.2 °C. Pt/C catalysts were prepared by dispersing 2 mg of Pt/C (20 wt% Pt on Vulcan XC-72) in 500 µL of EtOH with 17.5 µL of 5 wt% Nafion solution.[38] Then 300 µL of the catalyst ink was loaded onto CFP surface (0.5 × 0.5 cm^2) and air-dried at room temperature.

Determination of Band Gap: To investigate the E_c and E_v levels of CFP/$NiCo_2O_4$/CuS, UPS was used to determine the ionization potential (equivalent to E_v) of the samples (Figure S5, Supporting Information), which was calculated by subtracting the width of the He I UPS spectra from the excitation energy (21.22 eV). The band gaps of the catalysts were measured with the UV–vis method (Figure S6, Supporting Information). The incorporation of CuS into the CFP/$NiCo_2O_4$ leads to a UV–vis absorption over the entire wavelength range investigated (Figure S6a, Supporting Information). The optical band gap of a semiconductor can be estimated from the Tauc plot (i.e., the curve of converted $(\alpha h\nu)^r$ versus $h\nu$ from the UV–vis spectrum, in which α, h, and ν are the absorption coefficient, Planck constant, and light frequency, respectively, and $r = 2$ for a direct band gap material and $r = 1/2$ for an indirect band gap material). The E_g value of CFP/$NiCo_2O_4$ was thus determined by measuring the x-axis intercept of an extrapolated line from the linear regime of the curve (Figure S6b, black curve, Supporting Information).[28] The E_g value of CFP/$NiCo_2O_4$/CuS was thus determined by measuring the x-axis intercept of an extrapolated line from the linear regime of the curve (Figure S6b, red curve, Supporting Information).

Determination of FE: The FE was calculated by comparing the amount of measured hydrogen generated by potentiostatic cathodic electrolysis with calculated hydrogen (assuming 100% FE). The total amount of charge (Q) passed through the cell was obtained from the current–time curve. The total amount of H_2 produced (n) was measured using the pressure sensor. Assuming two electrons are needed to make one H_2 from two protons. $FE = 2Fn/Q$.

Active Sites Calculation: The number of active sites (n) is examined using CVs with pH = 7 phosphate buffer at a scan rate of 50 mV s^{-1}. When the number of voltammetric charges (Q) is obtained after deduction of the blank value, n (mol) can be calculated with the following equation[39]

$$n = Q/2F$$

where F is Faraday constant (96485 C mol^{-1}). For the sample of CFP/$NiCo_2O_4$/CuS, Q is 3.347×10^{-2} C (obtained from Figure S9a, Supporting Information), n (mol) = $3.347 \times 10^{-2} / (2 \times 96485)$ mol = 1.73×10^{-7} mol. TOF (s^{-1}) is calculated with the following equation[39]

$$\text{TOF} = I / (2Fn)$$

where I (A) is the current of the polarization curve obtained from the LSV measurements.

Supporting Information

Supporting Information is available from the Wiley Online Library or from the author.

Acknowledgements

L.A. and L.H. contributed equally to this work. The authors acknowledge support from the National Natural Science Foundation of China (Grant Nos. 21571089, 21201092, 21403097 and 21501081), National Fund for Talent Training in Basic Science of China (Grant No. J1103307), and the Fundamental Research Funds for the Central Universities (Lzujbky-2014-m02, Lzujbky-2015-19 and lzujbky-2014-182).

Received: September 7, 2015
Published online: October 7, 2015

[1] a) J. Kibsgaard, Z. B. Chen, B. N. Reinecke, T. F. Jaramillo, *Nat. Mater.* **2012**, *11*, 963; b) H. M. Chen, C. K. Chen, R. S. Liu, L. Zhang, J. J. Zhang, D. P. Wilkinson, *Chem. Soc. Rev.* **2012**, *41*, 5654; c) Y. Jiang, X. Li, S. Yu, L. Jia, X. Zhao, C. Wang, *Adv. Funct. Mater.* **2015**, *18*, 2693.

[2] a) M. S. Dresselhaus, I. L. Thomas, *Nature* **2001**, *414*, 332; b) R. Subbaraman, D. Tripkovic, D. Strmcnik, K. C. Chang, M. Uchimura, A. P. Paulikas, V. Stamenkovic, N. M. Markovic, *Science* **2011**, *334*, 1256; c) A. Kudo, Y. Miseki, *Chem. Soc. Rev.* **2009**, *38*, 253; d) Z. Zhuang, W. Sheng, Y. Yan, *Adv. Mater.* **2014**, *23*, 3950; e) L. Jia, X. Sun, Y. Jiang, S. Yu, C. Wang, *Adv. Funct. Mater.* **2015**, *12*, 1814.

[3] a) X. Zou, X. Huang, A. Goswami, R. Silva, B. R. Sathe, E. Mikmeková, T. Asefa, *Angew. Chem. Int. Ed.* **2014**, *53*, 4372; b) M. A. Lukowski, A. S. Daniel, F. Meng, A. Forticaux, L. Li, S. Jin, *J. Am. Chem. Soc.* **2013**, *135*, 10274; c) M. S. Faber, R. Dziedzic, M. A. Lukowski, N. S. Kaiser, Q. Ding, S. Jin, *J. Am. Chem. Soc.* **2014**, *136*, 10053.

[4] a) B. Fang, J. Kim, J. S. Yu, *Electrochem. Commun.* **2008**, *10*, 659; b) Z. Varpness, J. W. Peters, M. Young, T. Douglas, *Nano Lett.* **2005**, *5*, 2306; c) S. A. Grigoriev, P. Millet, V. N. J. Fateev, *Power Sources* **2008**, *177*, 281.

[5] a) A. L. Goff, V. Artero, B. Jousselme, P. D. Tran, N. Guillet, R. Métayé, A. Fihri, S. Palacin, M. Fontecave, *Science* **2009**, *326*, 1384; b) M. Hambourger, M. Gervaldo, D. Svedruzic, P. W. King, D. Gust, M. Ghirardi, A. L. Moore, T. A. Moore, *J. Am. Chem. Soc.* **2008**, *130*, 2015; c) Z. Chai, C. Wang, H. Zhang, C. M. Doherty, B. P. Ladewig, A. J. Hill, H. Wang, *Adv. Funct. Mater.* **2010**, *24*, 4394.

[6] a) Y. Liu, G. Yu, G.-D. Li, Y. Sun, T. Asefa, W. Chen, X. Zou, *Angew. Chem. Int. Ed* **2015**, *54*, 10752; b) S. Gao, G.-D. Li, Y. Liu, H. Chen, L.-L. Feng, Y. Wang, M. Yang, D. Wang, S. Wang, X. Zou, *Nanoscale* **2015**, *7*, 2306; c) X. Zou, Y. Zhang, *Chem. Soc. Rev.* **2015**, *44*, 5148.

[7] a) E. Casado-Rivera, D. J. Volpe, L. Alden, C. Lind, C. Downie, T. Vázquez-Alvarez, A. C. D. Angelo, F. J. DiSalvo, H. D. Abruña, *J. Am. Chem. Soc.* **2004**, *126*, 4043; b) H. Jin, J. Wang, D. Su, Z. Wei, Z. Pang, Y. Wang. *J. Am. Chem. Soc.* **2015**, *137*, 2688; c) S. Han, Y. Feng, F. Zhang, C. Yang, Z. Yao, W. Zhao, F. Qiu, L. Yang, Y. Yao, X. Zhuang, X. Feng, *Adv. Funct. Mater.* **2015**, *25*, 3899.

[8] a) M. W. Kanan, D. G. Nocera, *Science* **2008**, *321*, 1072; b) G. S. Hutchings, Y. Zhang, J. Li, B. T. Yonemoto, X. Zhou, K. Zhu, F. Jiao, *J. Am. Chem. Soc.* **2015**, *137*, 4223; c) J. Rosen, G. S. Hutchings, F. Jiao, *J. Am. Chem. Soc.* **2013**, *135*, 4516; d) Z. Zhuang, W. Sheng, Y. Yan, *Adv. Mater.* **2014**, *23*, 3950.

[9] a) C.-H. Lin, C.-L. Chen, J.-H. Wang, *J. Phys. Chem. C* **2011**, *115*, 18582; b) C. Lupi, A. Dell'Era, M. Pasquali, *Int. J. Hydrogen Energy* **2009**, *34*, 2101.

[10] a) Y. Li, P. Hasin, Y. Wu, *Adv. Mater.* **2010**, *22*, 1926; b) H. Shi, G. Zhao, *J. Phys. Chem. C* **2014**, *45*, 25939.

[11] a) R. Chen, H.-Y. Wang, J. Miao, H. Yang, B. Liu, *Nano Energy* **2015**, *11*, 333; b) H. Shi, G. Zhao, *J. Phys. Chem. C* **2014**, *45*, 25939; c) P. Xiao, X. Ge, H. Wang, Z. Liu, A. Fisher, X. Wang, *Adv. Mater.* **2015**, *25*, 1520.

[12] a) M. S. Faber, R. Dziedzic, M. A. Lukowski, N. S. Kaiser, Q. Ding, S. Jin, *J. Am. Chem. Soc.* **2014**, *136*, 10053; b) P. Jiang, Q. Liu, Y. Liang, J. Tian, A. M. Asiri, X. Sun, *Angew. Chem. Int. Ed.* **2014**, *126*, 13069.

[13] a) E. J. Popczun, C. G. Read, C. W. Roske, N. S. Lewis, R. E. Schaak, *Angew. Chem. Int. Ed.* **2014**, *53*, 5427; b) Y. Xu, M. Gao, Y. Zheng, J. Jiang, S. Yu, *Angew. Chem. Int. Ed.* **2013**, *52*, 8546; c) Y. Hou, A. B. Laursen, J. Zhang, G. Zhang, Y. Zhu, X. Wang, S. Dahl, I. Chorkendorff, *Angew. Chem. Int. Ed.* **2013**, *52*, 3621.
[14] a) D. Kong, J. Cha, H. Wang, H. R. Lee, Y. Cui, *Energy Environ. Sci.* **2013**, *6*, 3553; b) P. D. Tran, S. Y. Chiam, P. P. Boix, Y. Ren, S. S. Pramana, J. Fize, V. Artero, J. Barber, *Energy Environ. Sci.* **2013**, *6*, 2452.
[15] B. Hinnemann, P. G. Moses, J. Bonde, K. P. Jørgensen, J. H. Nielsen, S. Horch, I. Chorkendorff, J. K. Nørskov, *J. Am. Chem. Soc.* **2005**, *127*, 5308.
[16] T. F. Jaramillo, K. P. Jørgensen, J. Bonde, J. H. Nielsen, S. Horch, I. Chorkendorff, *Science* **2007**, *317*, 100.
[17] J. Xie, J. Zhang, S. Li, F. Grote, X. Zhang, H. Zhang, R. Wang, Y. Lei, B. Pan, Y. Xie, *J. Am. Chem. Soc.* **2013**, *135*, 17881.
[18] S. Conejeros, I. P. R. Moreira, P. Alemany, E. Canadell, *Inorg. Chem.* **2014**, *53*, 12402.
[19] a) X. Zhang, Y. Xie, *Chem. Soc. Rev.* **2013**, *42*, 8187; b) J. Feng, X. Sun, C. Wu, L. Peng, C. Lin, S. Hu, J. Yang, Y. Xie, *J. Am. Chem. Soc.* **2011**, *133*, 17832; c) J. Xie, X. Sun, N. Zhang, K. Xu, M. Zhou, Y. Xie, *Nano Energy* **2013**, *2*, 65.
[20] a) N. Ding, N. Yan, C. Ren, X. Chen, *Anal. Chem.* **2010**, *82*, 5897; b) M. Gao, Y. Xu, J. Jiang, S. Yu, *Chem. Soc. Rev.* **2013**, *42*, 2986; c) W. Du, X. Qian, X. Ma, Q. Gong, H. Cao, *Chem. Eur. J.* **2007**, *13*, 3241.
[21] a) J. Liang, Z. Fan, S. Chen, S. Ding, G. Yang, *Chem. Mater.* **2014**, *26*, 4354; b) Y.-H. Chang, C.-T. Lin, T.-Y. Chen, C.-L. Hsu, Y.-H. Lee, W. Zhang, K.-H. Wei, L.-J. Li, *Adv. Mater.* **2013**, *5*, 567.
[22] a) X. Zhang, Y. Xie, *Chem. Soc. Rev.* **2013**, *42*, 8187; b) J. Feng, X. Sun, C. Wu, L. Peng, C. Lin, S. Hu, J. Yang, Y. Xie, *J. Am. Chem. Soc.* **2011**, *133*, 17832; c) J. Xie, X. Sun, N. Zhang, K. Xu, M. Zhou, Y. Xie, *Nano Energy* **2013**, *2*, 65; d) J. Duan, S. Chen, B. A. Chambers, G. G. Andersson, S. Z. Qiao, *Adv. Mater.* **2015**, *27*, 4234.
[23] L. Huang, D. Chen, Y. Ding, S. Feng, Z. L. Wang, M. Liu, *Nano Lett.* **2013**, *13*, 3135.
[24] a) P. Manivasakan, P. Ramasamy, J. Kim, *Nanoscale* **2014**, *6*, 9665; b) R. Zou, K. Xu, T. Wang, G. He, Q. Liu, X. Liu, Z. Zhang, J. Hu, *J. Mater. Chem. A* **2013**, *1*, 8560; c) R. Ding, L. Qi, M. Jia, H. Wang, *Catal. Sci. Technol.* **2013**, *3*, 3207.
[25] A. B. F. Martinson, S. C. Riha, E. Thimsen, J. W. Elam, M. J. Pellin, *Energy Environ. Sci.* **2013**, *6*, 1868.
[26] a) D. Lee, J. Kim, *Thin Solid Films* **2010**, *518*, 6537; b) M. Ishii, K. Shibata, H. Nozaki, *J. Solid State Chem.* **1993**, *105*, 504.
[27] J. Xie, J. Zhang, S. Li, F. Grote, X. Zhang, H. Zhang, R. Wang, Y. Lei, B. Pan, Y. Xie, *J. Am. Chem. Soc.* **2013**, *135*, 17881.
[28] J. Liu, Y. Liu, N. Liu, Y. Han, X. Zhang, H. Huang, Y. Lifshitz, S. T. Lee, J. Zhang, Z. Kang, *Science* **2015**, *347*, 970.
[29] a) B. E. Conway, B. V. Tilak, *Electrochim. Acta* **2002**, *47*, 3571; b) Y.-F. Xu, M.-R. Gao, Y.-R. Zheng, J. Jiang, S. H. Yu, *Angew. Chem. Int. Ed.* **2013**, *52*, 8546.
[30] a) E. J. Popczun, J. R. McKone, C. G. Read, A. J. Biacchi, A. M. Wiltrout, N. S. Lewis, R. E. Schaak, *J. Am. Chem. Soc.* **2013**, *135*, 9267; b) Z. Xing, Q. Liu, A. M. Asiri, X. Sun, *Adv. Mater.* **2014**, *32*, 5702.
[31] D.-J. Guo, X.-P. Qiu, W.-T. Zhu, L.-Q. Chen, *Appl. Catal. B: Environ.* **2009**, *89*, 597.
[32] F. Song, X. Hu, *J. Am. Chem. Soc.* **2014**, *136*, 16481.
[33] D. Merki, S. Fierro, H. Vrubel, X. Hu, *Chem. Sci.* **2011**, *2*, 1262.
[34] T. F. Jaramillo, K. P. Jørgensen, J. Bonde, J. H. Nielsen, S. Horch, I. Chorkendorff, *Science* **2007**, *317*, 100.
[35] a) J. Xie, H. Zhang, S. Li, R. Wang, X. Sun, M. Zhou, J. Zhou, X. Lou, Y. Xie, *Adv. Mater.* **2013**, *25*, 5807; b) S. Xu, D. Li, P. Wu, *Adv. Mater.* **2015**, *25*, 1127.
[36] J. Tian, Q. Asiri, A. M. Liu, X. Sun, *J. Am. Chem. Soc.* **2014**, *136*, 7587.
[37] J. Tian, Q. Liu, Y. Liang, Z. Xing, A. M. Asiri, X. Sun, *ACS Appl. Mater. Interfaces* **2014**, *6*, 20579.
[38] a) Z. Li, A. L. K. Lui, K. H. Lam, L. Xi, Y. M. Lam, *Inorg. Chem.* **2014**, *53*, 10874; b) A. J. Bard, L. R. Faulkner, *Electrochemical Methods: Fundamentals and Applications*, Wiley, New York **1980**.
[39] M.-R. Gao, X. Cao, Q. Gao, Y.-F. Xu, Y.-R. Zheng, J. Jiang, S.-H. Yu, *ACS Nano* **2014**, *8*, 3970.